
This is the **submitted version** of the journal article:

Yang, Dawei; Li, Mengyao; Zheng, Xuejiao; [et al.]. «Phase engineering of defective copper selenide toward robust lithium-sulfur batteries». ACS nano, Vol. 16, issue 7 (July 2022), p. 11102-11114. DOI 10.1021/acsnano.2c03788

This version is available at <https://ddd.uab.cat/record/270834>

under the terms of the  **IN**
COPYRIGHT license

Synergistically Enhancement of Electrochemical Kinetics by Phase Engineering of Defective Copper Selenide toward Robust Lithium-Sulfur Batteries

Dawei Yang,^{†,‡} Mengyao Li,^{,†,‡} Xuejiao Zheng,[&] Xu Han,[§] Chaoqi Zhang,^{†,‡} Jordi Jacas Biendicho,[†] Jordi Llorca,^{//} Jiaao Wang,^{*,§} Hongchang Hao,[±] Junshan Li,[°] Graeme Henkelman,[§] Jordi Arbiol,^{§,⊥} Joan Ramon Morante,^{†,‡} David Mitlin,^{*,±} Shu-Lei Chou,^{*,#} Andreu Cabot^{*,†,⊥}*

[†] Catalonia Institute for Energy Research – IREC, Sant Adrià de Besòs, Barcelona, 08930, Spain.

[‡] Department of Electronic and Biomedical Engineering, Universitat de Barcelona, 08028, Barcelona, Spain.

[&] Nanjing Hydraulic Research Institute, Nanjing 210029, China.

[§] Catalan Institute of Nanoscience and Nanotechnology (ICN2), CSIC and BIST, Campus, UAB, Bellaterra, 08193, Barcelona, Spain.

^{//} Institute of Energy Technologies, Department of Chemical Engineering and Barcelona Research Center in Multiscale Science and Engineering, Universitat Politècnica de Catalunya, EEBE, 08019, Barcelona, Spain.

[§] Department of Chemistry and the Oden Institute for Computational Engineering and Sciences, The University of Texas at Austin, Austin, TX, 78712 USA.

1
2
3
4 [±] Materials Science and Engineering Program & Texas Materials Institute, The University of
5
6 Texas at Austin, Austin, Texas 78712, United States.
7

8
9 [°] Institute of Advanced Study, Chengdu University, 610106, Chengdu, China.
10

11
12 [#] Institute for Carbon Neutralization, College of Chemistry and Materials Engineering,
13
14 Wenzhou University, Wenzhou, Zhejiang 325035, China.
15

16
17 [⊥] ICREA, Pg. Lluís Companys 23, 08010, Barcelona, Spain.
18

19
20 Email: limengyao@irec.cat
21

22
23 Email: wangjiaao0720@utexas.edu
24

25
26 Email: david.mitlin2@utexas.edu
27

28
29 Email: chou@wzu.edu.cn
30

31
32 Email: acabot@irec.cat
33
34
35
36

37 **Abstract**

38
39 The shuttling of soluble lithium polysulfides (LiPS) and the sluggish Li-S conversion kinetics
40
41 are two main barriers toward the practical application of lithium-sulfur batteries (LSBs). Herein,
42
43 we propose the addition of copper selenide nanoparticles at the cathode to trap LiPS and
44
45 accelerate the Li-S reaction kinetics. Using both computational and experimental results, we
46
47 demonstrate the crystal phase and concentration of copper vacancies to control the electronic
48
49 structure of the copper selenide, its affinity towards LiPS chemisorption, and its electrical
50
51 conductivity. The adjustment of the defect density also allows tuning the electrochemically
52
53 active sites for the catalytic conversion of polysulfide. The optimized S/Cu_{1.8}Se cathode
54
55 efficiently promotes and stabilizes the sulfur electrochemistry, thus improving significantly the
56
57
58
59
60

1
2
3
4
5
6
7
8
9
10
11
12
13
14
15
16
17
18
19
20
21
22
23
24
25
26
27
28
29
30
31
32
33
34
35
36
37
38
39
40
41
42
43
44
45
46
47
48
49
50
51
52
53
54
55
56
57
58
59
60

LSB performance, including an outstanding cyclability over 1000 cycles at 3 C with a capacity fading rate of just 0.029% per cycle, a superb rate capability up to 5 C, and a high areal capacity of 6.07 mAh cm⁻² under high sulfur loading. Overall, the present work proposes a crystal phase and defect engineering strategy toward fast and durable sulfur electrochemistry, demonstrating great potential in developing practical LSBs.

Keywords: Copper selenide, phase engineering, copper vacancies, lithium-sulfur battery, lithium polysulfide

Lithium-sulfur battery (LSB) has emerged as one of the most promising energy storage technologies owing to its large energy density (2600 Wh kg^{-1}) and high potential for low cost and environmental friendliness.¹⁻³ Despite these attractive advantages, the deployment of commercial LSBs is still hampered by several limitations, including the intrinsically low conductivity of sulfur and lithium sulfides, the dissolution and shuttling of lithium polysulfide (LiPS) intermediates, the large volume change of sulfur during the charge-discharge process, and the slow Li-S reaction kinetics, which result in insufficient cycling stabilities and rate capabilities.⁴⁻⁶

To address these issues, extensive efforts have been devoted to synthesizing porous/hollow carbon-based cathode hosts to physically confine sulfur and polysulfides.⁷⁻¹⁰ However, the shuttle effect of soluble polysulfides cannot be effectively suppressed by means of carbon encapsulation due to the weak interaction of LiPS with nonpolar carbon materials. Beyond encapsulation, a more effective strategy to suppress the shuttle effect is the use of sulfur host materials able to chemisorb and catalyze the LiPS reaction. In this direction, several polar inorganic compounds including metal oxides,^{11,12} nitrides,¹³ phosphides,¹⁴ and sulfides¹⁵ have been incorporated into the host to chemically immobilize polysulfide species, accelerate their conversion, and thus reduce their dissolution and shuttling. Among the proposed compounds, transition metal chalcogenides (TMCs) have been demonstrated particularly effective.^{16,17}

Copper chalcogenides have recently drawn extensive attention as functional materials in several energy conversion and storage applications, including photovoltaics, thermoelectrics and several electrochemical technologies.¹⁸⁻²⁰ The suitability of copper chalcogenides arises from the abundance of their constituent elements, the strong influence of Cu 3d states on the

1
2
3
4 electronic band structure near the Fermi level, the contribution of the redox reactions between
5
6 Cu^0 , Cu^{1+} and Cu^{2+} to catalytically activating several processes, and the low defect formation
7
8 energies that result in large densities of defects that control the optical, charge transport and
9
10 catalytic properties of the material.^{21,22}
11
12

13
14 Among the different copper chalcogenides, sulfides offer advantages in terms of cost but are
15
16 characterized by moderate electrical conductivities. At the other extreme, copper telluride
17
18 shows a metallic character, but the low abundance of tellurium prevents its use in applications
19
20 involving large volumes of material. Selenides thus represent the best compromise, as
21
22 recognized in the fields of photovoltaics and thermoelectrics among others. Copper selenides
23
24 have been also recently reported to show excellent electrocatalytic activity towards the oxygen
25
26 reduction reaction among other electrocatalytic reactions.^{23,24}
27
28
29

30
31 In the field of LSBs, copper sulfides have been explored as sulfur hosts able to expedite the
32
33 polysulfides transformation, with notable success.²⁵⁻²⁸ On the other hand, surprisingly, despite
34
35 its high potential as LiPS adsorbent and Li-S electrocatalysts, no previous work on the use of
36
37 copper selenides as sulfur host in LSB cathodes has been reported.
38
39

40
41 Herein, we produced copper selenide electrocatalyst and optimized them towards the LiPS
42
43 adsorption and catalytic conversion through adjusting their crystal phase and Cu vacancy
44
45 concentration. Computational and experimental analyses are used to demonstrate that tailoring
46
47 the crystal phase and defect concentration allows modulating the electrical conductivity of the
48
49 material, its chemical affinity towards LiPS adsorption, and its catalytic activity towards LiPS
50
51 conversion reactions. The optimized materials are loaded with sulfur and tested as cathode
52
53 material in LSBs, which capacity, stability and rate capability are thoroughly investigated.
54
55
56
57
58
59
60

RESULTS AND DISCUSSION

A rapid synthetic protocol based on the injection of TOPSe complex into a copper precursor solution at 220 °C was developed to produce the copper selenide NPs, as schematized in Scheme1 (see details in the experimental section).

Figures 1a and S1 display TEM images of the 20 ± 10 nm quasi-spherical NPs obtained. EELS chemical composition maps displayed a uniform distribution of Cu and Se within each particle (Figure 1c). HRTEM characterization showed the crystal structure of the NPs to match the $\text{Cu}_{1.8}\text{Se}$ cubic phase (Figure 1b).²⁹ XRD patterns confirmed the cubic $\text{Cu}_{1.8}\text{Se}$ phase (JCPDS No. 01-071-0044, Figure 1g).²⁹

$\text{Cu}_{1.8}\text{Se}$ NPs were annealed in a reducing atmosphere at 600°C for 3h. Figures 1d,f and S2 display TEM and HRTEM images of the annealed material, which was characterized by larger crystal domains of a different phase identified as orthorhombic Cu_2Se .³⁰ XRD analysis confirmed the crystal structure of the annealed material to match that of orthorhombic Cu_2Se (JCPDS No. 00-019-0401, Figure 1g).³⁰ EELS chemical composition maps displayed a uniform distribution of Cu and Se within the Cu_2Se sample (Figure 1e).

Figure 1h displays the high-resolution Cu 2p XPS spectra of $\text{Cu}_{1.8}\text{Se}$ and Cu_2Se . A unique Cu 2p doublet was identified from both samples and it was associated with Cu^+ within a copper selenide environment.³¹ The Cu 2p doublet was located at 954.5 ($2p_{1/2}$) and 934.5 eV ($2p_{3/2}$) in Cu_2Se , and it was slightly shifted toward lower binding energies in $\text{Cu}_{1.8}\text{Se}$. The Se 3d XPS spectra of $\text{Cu}_{1.8}\text{Se}$ and Cu_2Se also displayed a single chemical state ascribed Se^{2-} , with a unique doublet located at 54.3 eV ($3d_{3/2}$) and 53.2 eV ($3d_{5/2}$) in the case of Cu_2Se and shifted to slightly higher energies in $\text{Cu}_{1.8}\text{Se}$.^{32,33} The correlated redshift of the Cu 2p spectrum and blue shift of

the Se 3d spectrum when decreasing the Cu:Se ratio from Cu_2Se to $\text{Cu}_{1.8}\text{Se}$ is associated with a transfer of charge from Se to Cu.

Sulfur was introduced within the host materials by a melt-diffusion process (see the experimental section for details). XRD patterns confirmed the presence of crystalline sulfur (JCPDS No. 01-85-0799) within the $\text{S}/\text{Cu}_{1.8}\text{Se}$ composites (Figure S3).³⁴ EELS elemental maps displayed a homogeneous distribution of the three elements, Cu, Se and S, within the composite (Figure 1j), with no independent sulfur particle. Nitrogen adsorption-desorption isotherms showed the Brunauer–Emmett–Teller (BET) specific surface area to be reduced from $64.3 \text{ m}^2 \text{ g}^{-1}$ for $\text{Cu}_{1.8}\text{Se}$ to $9.5 \text{ m}^2 \text{ g}^{-1}$ for $\text{S}/\text{Cu}_{1.8}\text{Se}$, which further demonstrated the successful loading of sulfur (Figure S4). Thermogravimetric analysis (TGA) allowed quantifying the sulfur content in the $\text{S}/\text{Cu}_{1.8}\text{Se}$ composite at about 70.0 wt%, consistent with the nominal amount introduced (Figure S5).

To evaluate LiPS adsorption affinity, the same amount of the different hosts was immersed into a 0.01 M Li_2S_4 solution. After 12 h, clear differences in the colour of the solutions containing the different materials were appreciated both by direct observation and using UV-vis spectroscopy, indicating a different degree of LiPS adsorption (Figure 2a,b). As observed from the optical images in Figure 2a, the 0.01 M Li_2S_4 solution had an intense orange colour. In the presence of the carbon black Super P, the colour of the solution remained unchanged after 12 h, as it was expected from the low affinity of the nonpolar carbon surface to LiPS. On the other hand, the two solutions containing copper selenides displayed a much more pallid colour, indicating that most of the Li_2S_4 in the solution had been captured by the adsorber. More precise conclusions can be obtained from the UV-vis spectra (Figure 2b). Li_2S_4 presents a strong

absorption band in the range of 400-500 nm.^{35,36} The absorbance in this region strongly decreased in the presence of Cu₂Se, but especially with Cu_{1.8}Se, indicating a much stronger polysulfide adsorption ability of the latter.

The surface chemical states of Cu_{1.8}Se after the Li₂S₄ adsorption test (labelled as Cu_{1.8}Se-Li₂S₄) were analyzed and compared with those of pristine Cu_{1.8}Se. Figure 2c displays the high-resolution Cu 2p XPS spectra of Cu_{1.8}Se-Li₂S₄. Compared with Cu_{1.8}Se, the Cu 2p spectrum of Cu_{1.8}Se-Li₂S₄ shifted toward lower binding energies, which is attributed to the less electronegative chemical environment created by the chemical adsorption of negatively charged polysulfide species on the Cu_{1.8}Se surface.³⁷ Besides, a second Cu 2p doublet was identified in the Cu 2p spectra of Cu_{1.8}Se-Li₂S₄, at 951.2 eV and 931.3 eV, corresponding to the 2p_{1/2} and 2p_{3/2} levels of Cu⁰. Thus a partial reduction of the surface copper ions in Cu_{1.8}Se took place during the LiPS chemisorption process.³¹ Figure 2d shows the high-resolution Se 3d spectrum of Cu_{1.8}Se before and after Li₂S₄ adsorption (Cu_{1.8}Se-Li₂S₄). Compared with pristine Cu_{1.8}Se, the Se 3d XPS spectrum of Cu_{1.8}Se-Li₂S₄ shifted to higher binding energies, which indicated an increase of the chemical environment electronegativity during the LiPS adsorption and simultaneous Cu partial reduction.^{38,39} The Li 1s XPS spectra of Cu_{1.8}Se-Li₂S₄ is compared with that of Li₂S₄ in Figure 2e. While the Li 1s band at 55.2 eV is attributed to the Li-S bonding within Li₂S₄, the new peak appearing in the Li 1s XPS spectra of Cu_{1.8}Se-Li₂S₄ is associated with the formation of Li-Se chemical bonds during the adsorption process.⁴⁰ Overall, the significant variations in the XPS spectra of Cu_{1.8}Se before and after the Li₂S₄ adsorption test clearly demonstrate the chemical interaction and thus affinity between the Cu_{1.8}Se surface and Li₂S₄.

DFT calculations were conducted to assess the affinity between LiPS species and $\text{Cu}_{1.8}\text{Se}$ and Cu_2Se . The calculated geometrically stable configurations of $\text{Cu}_2\text{Se}-\text{Li}_2\text{S}_4$ and $\text{Cu}_{1.8}\text{Se}-\text{Li}_2\text{S}_4$ are illustrated in Figure 2f. The results revealed that the S and Li atoms in Li_2S_4 preferentially bind with the Cu and Se atoms on the (002) surface of Cu_2Se and (111) surface of $\text{Cu}_{1.8}\text{Se}$, respectively. While in both cases negative binding energies were obtained, a significantly higher absolute value of the binding energy (-3.21 eV) is achieved for $\text{Cu}_{1.8}\text{Se}-\text{Li}_2\text{S}_4$ than for $\text{Cu}_2\text{Se}-\text{Li}_2\text{S}_4$ (-1.62 eV), which is consistent with the Li_2S_4 test results.

To gain additional insight into the interactions between LiPS species and copper selenide surfaces, the charge density difference of Li_2S_4 species adsorbed on Cu_2Se (220) and $\text{Cu}_{1.8}\text{Se}$ (111) were calculated and are displayed in Figure 2g. The cyan isosurfaces around the Li-S bonds in Li_2S_4 indicated a decreased charge density and weakened bonds between Li and S atoms, which benefits its further conversion toward lower-order LiPS. In addition, the yellow isosurface suggests that the charge density between $\text{Cu}_{1.8}\text{Se}$ and the Li atom of Li_2S_4 was significantly increased, indicating a strong interaction between $\text{Cu}_{1.8}\text{Se}$ and Li_2S_4 , which is consistent with the stronger affinity of the $\text{Cu}_{1.8}\text{Se}$ surfaces to LiPS.⁴¹

The results of computational simulations of the interactions between Cu_xSe and different LiPS covering the full range of sulfur chemical states upon battery operation (Li_2S , Li_2S_2 , Li_2S_4 , Li_2S_6 , Li_2S_8 , and S_8) are displayed in Figure S6 and S7. The S-Cu and Li-Se attractions can be confirmed and are maintained in all the LiPS-adsorbent couples, while $\text{Cu}_{1.8}\text{Se}$ exhibits stronger adsorbability for the LiPS by showing systematically higher binding energies (Figure 2h) and shorter bond lengths for both the S-Cu and Li-Se bonds than Cu_2Se (Figure S8).

DFT results showed the $\text{Cu}_{1.8}\text{Se}$ Fermi level to lay within a band of states, which was consistent with its degenerated/metallic character and is related to the high density of Cu vacancies that provide high hole densities.^{33,42} In contrast, the Fermi level of Cu_2Se lies within its bandgap showing a p-type semiconductor behaviour (Figure 3a).

DFT calculations were also used to evaluate the lithium-ion and Li_2S_4 diffusion on the (002) facet of Cu_2Se and the (111) facet of $\text{Cu}_{1.8}\text{Se}$. The geometrical configurations of the Li-ion diffusion paths are shown in Figure 3b and the corresponding energy profiles are displayed in Figure 3c. The calculated Li-ion diffusion energy barriers (E_{barrier}) were relatively low, just 0.34 eV for Cu_2Se and even a threefold smaller, 0.11 eV, for $\text{Cu}_{1.8}\text{Se}$. Figure 3d,e displays the geometrical configurations of the path for Li_2S_4 migration on the (002) facet of Cu_2Se and the (111) facet of $\text{Cu}_{1.8}\text{Se}$ and the E_{barrier} for Li_2S_4 migration along different adsorption sites. Calculations showed the E_{barrier} for Li_2S_4 migration on Cu_2Se to be 0.89 eV and just 0.30 eV on $\text{Cu}_{1.8}\text{Se}$. These low diffusion barriers allow fast Li-ion and LiPS diffusion rates on the copper selenide surfaces, which promotes the Li - S redox reactions.

Figure 3f exhibits the initial state, transition state, and final state of Li_2S decomposition based on different sulfur hosts. The calculated energy barrier for Li_2S decomposition on Cu_2Se and $\text{Cu}_{1.8}\text{Se}$ surfaceS was 1.27 and 0.63 eV, respectively (Figure 3g). Thus, the defective cubic $\text{Cu}_{1.8}\text{Se}$ can greatly reduce the Li_2S decomposition energy barrier and enhance the redox reversibility between Li_2S and LiPS.

The calculated Gibbs free energy changes during the S reduction on Cu_2Se and $\text{Cu}_{1.8}\text{Se}$ are displayed in Figure 3h. The overall reversible reaction from S_8 and Li to Li_2S was considered. During the discharge process, the first step involves the double reduction of S_8 with two Li^+ to

form Li_2S_8 . Then Li_2S_8 undergoes further reduction to three intermediate LiPS, Li_2S_6 , Li_2S_4 , and Li_2S_2 . Finally, Li_2S is obtained as the end product. The largest increase of Gibbs free energy was obtained for the conversion from Li_2S_2 to Li_2S , suggesting this step as the rate-limiting one during the discharge process.^{43,44} Both copper selenides exhibited low Gibbs free energy changes, demonstrating their potential as Li-S catalysts. Among them, $\text{Cu}_{1.8}\text{Se}$ was characterized with the lowest Gibbs free energy change, 0.62 eV, well below that of Cu_2Se , 0.96 eV, which suggests that the reduction of S is more thermodynamically favourable on $\text{Cu}_{1.8}\text{Se}$ than on Cu_2Se . Overall, DFT calculations pointed at the defective cubic $\text{Cu}_{1.8}\text{Se}$ structure as the most effective to trap LiPS and catalytically accelerate the Li-S reversible reaction.

To experimentally evaluate the ability of host materials to catalytically accelerate the kinetics of polysulfide conversion, CV tests of Li_2S_6 symmetrical cells were conducted in the voltage window -0.8 to 0.8 V. As shown in Figure 4a, $\text{Cu}_{1.8}\text{Se}$, Cu_2Se , and Super P electrodes showed significantly different CV curves. The symmetric curves of $\text{Cu}_{1.8}\text{Se}$ electrodes exhibited higher peak current densities than Cu_2Se and Super P electrodes, illustrating the faster reaction kinetics of $\text{Cu}_{1.8}\text{Se}$ during liquid-to-solid ($\text{Li}_2\text{S} \leftrightarrow \text{S}_6^{2-} \leftrightarrow \text{S}_8$) conversion.^{16,45} When similar experiments were carried out on $\text{Cu}_{1.8}\text{Se}$ electrodes without Li_2S_6 addition in the electrolyte, approximately linear-shaped CV curves were obtained, pointing at a pure capacitive behaviour rather than a chemical reaction. This result implies that Li_2S_6 was the sole electrochemically active species in the system. The well-maintained CV profile of symmetric cells based on $\text{Cu}_{1.8}\text{Se}$ after 10 cycles points at proper reaction stability (Figure S9).

The electrochemical performance of the electrodes was evaluated using coin-type cells. Figure 4b displays the CV profiles of Li-S cells based on S/Cu_{1.8}Se, S/Cu₂Se and S/Super P cathodes at a scan rate of 0.1 mV s⁻¹. All curves displayed two reduction peaks (peak C1 and C2) that were attributed to a two-step S reduction process upon cathodic scanning: peak C1 was associated with the transformation from sulfur to soluble long-chain LiPS (Li₂S_x, 4 ≤ x ≤ 8), and peak C2 to a further reduction of sulfur to insoluble Li₂S₂/Li₂S.^{46,47} The anodic peak (peak A) corresponded to the reverse multistep oxidation process of short-chain sulfides to LiPS and eventually to sulfur.⁴⁸ S/Cu_{1.8}Se electrodes exhibited the most intense peak currents and the most positive/negative potentials of the cathodic/anodic peaks (Figure 4c). This result indicates that among the tested materials, Cu_{1.8}Se was the most effective catalyst in promoting the polysulfides redox reaction kinetics.

The excellent catalytic activity of Cu_{1.8}Se was further confirmed by measuring the onset potentials at a current density of 10 μA cm⁻² beyond the baseline current (Figure S10).^{48,49} As illustrated in Figure 4c, among the three electrodes tested, S/Cu_{1.8}Se exhibited the highest onset potentials of reduction peaks and the lowest onset potentials of oxidation peaks, evidencing the ability of Cu_{1.8}Se to reduce the overpotentials of the Li-S reversible reaction. Besides, the CV curves of S/Cu_{1.8}Se almost overlapped, showing no obvious peak shift or current changes, which points to excellent stability and reversibility (Figure S11).

The lithium-ion (Li⁺) diffusion rate, which is another important factor affecting the conversion kinetics of LiPSs, was investigated by measuring CV curves at different scan rates, from 0.1 to 0.5 mV s⁻¹. Figure S12 displays the results obtained from S/Cu_{1.8}Se, S/Cu₂Se, and S/Super P electrodes containing similar amounts of sulfur. All reduction and oxidation peaks current were

observed to linearly change with the square root of the scan rates, demonstrating the reaction to be diffusion-limited. Thus the Li^+ diffusivity can be estimated according to the classical Randles-Sevcik equation:^{35,50}

$$I_p = (2.69 \times 10^5) n^{1.5} A D_{\text{Li}^+}^{0.5} C_{\text{Li}^+} \nu^{0.5}$$

where I_p is the peak current density, n is the number of reaction electrons, A is the geometric area of the electrode, D_{Li^+} is the Li^+ diffusion coefficient, C_{Li^+} is the concentration of Li^+ in the electrolyte, and ν is the scan rate.

As shown in Figure 4d-f, S/ $\text{Cu}_{1.8}\text{Se}$ electrodes exhibited the sharpest slopes for the three peaks (peak C1, peak C2, and peak A), thus the highest Li^+ diffusivity during the redox reactions. Based on the Randles-Sevcik equation, S/ $\text{Cu}_{1.8}\text{Se}$ electrodes were characterized by a D_{Li^+} at peaks C1, C2, and A of 3.3×10^{-7} , 5.0×10^{-7} , and $8.6 \times 10^{-7} \text{ cm}^2 \text{ s}^{-1}$, respectively, well above the values obtained for S/ Cu_2Se and S/Super P (Figure 4g). The Li^+ diffusivity strongly depends on the accumulation of insulating $\text{Li}_2\text{S}/\text{Li}_2\text{S}_2$ on the electrode and the viscosity of the electrolyte that varies with the concentration of soluble LiPS.⁴⁸ The highest Li^+ diffusivities obtained for the $\text{Cu}_{1.8}\text{Se}$ host reflect a more effective catalytic activity towards Li-S reaction and a more effective trapping of soluble LiPS that prevented them from dissolving into the electrolyte.

A very significant part of the discharge capacity, up to 75%, stems from the transformation of the Li_2S_4 intermediate into Li_2S . Thus the rate of Li_2S precipitation on the electrode matrix is a very significant conversion kinetic indicator for LSBs. From the potentiostatic discharge profiles in Figure 4h,i, both copper selenide electrodes displayed very sharp nucleation peaks and fast responsivity toward Li_2S nucleation, being the $\text{Cu}_{1.8}\text{Se}$ performance significantly better

than that of the Cu_2Se electrodes. According to Faraday's law, the Li_2S deposition capacity of $\text{Cu}_{1.8}\text{Se}$ (304 mAh g^{-1}) was larger than that of Cu_2Se (136 mAh g^{-1}).

Galvanostatic charge/discharge curves of $\text{S}/\text{Cu}_{1.8}\text{Se}$, $\text{S}/\text{Cu}_2\text{Se}$, and $\text{S}/\text{Super P}$ at 0.1 C ($1 \text{ C} = 1672 \text{ mA g}^{-1}$) exhibited one charge plateau and two discharge plateaus (Figure 5a), consistently with CV. The voltage gap between the charge plateaus and the second discharge is generally referred to as the polarization potential (ΔE).⁵¹ As displayed in Figure 5b, $\text{S}/\text{Cu}_{1.8}\text{Se}$ electrodes showed a lower polarization potential ($\Delta E = 150 \text{ mV}$) than $\text{S}/\text{Cu}_2\text{Se}$ ($\Delta E = 175 \text{ mV}$) and $\text{S}@ \text{Super P}$ electrodes ($\Delta E = 238 \text{ mV}$).

The catalytic activity of the host materials toward the LiPS conversion reaction can be further quantified by the ratio Q_H/Q_L , where Q_L and Q_H denote the capacity of the two discharge plateaus (Figure 5a). Q_L is related to the reduction of sulfur to soluble LiPS ($\text{S}_8 + 4\text{Li}^+ + 4\text{e}^- \rightarrow 2\text{Li}_2\text{S}_4$) and Q_H corresponds to the subsequent transformation to insoluble sulfide ($2\text{Li}_2\text{S}_4 + 12\text{Li}^+ + 12\text{e}^- \rightarrow 8\text{Li}_2\text{S}$).⁴³ Thus the ratio Q_H/Q_L can be interpreted in terms of the catalytic ability for LiPS conversion reaction: sluggish kinetics during the solid \rightarrow liquid \rightarrow solid process and shuttle effect caused by the diffusion of soluble LiPS give rise to capacity fading during Q_H stage. Thus, the higher Q_H/Q_L , the better the catalytic ability. As shown in Figure 5b, Q_H/Q_L ratios obtained for copper selenides were much larger than those of the carbon black ($Q_H/Q_L=1.71$), being the Q_H/Q_L ratio of the $\text{S}/\text{Cu}_{1.8}\text{Se}$ electrode ($Q_H/Q_L=2.71$) significantly larger than that of $\text{S}/\text{Cu}_2\text{Se}$ ($Q_H/Q_L=2.43$).

The electrochemical kinetics were further analyzed during the phase transformation between soluble LiPS and insoluble $\text{Li}_2\text{S}_2/\text{Li}_2\text{S}$ in the charge/discharge processes. Figure S13a shows the voltage jump at the initial charging period, reflecting the overpotentials of Li_2S activation.⁹

Besides, the galvanostatic discharge curves displayed a voltage dip at the beginning of the Li_2S precipitation voltage plateaus, which is associated with the overpotential of Li_2S nucleation (Figure S13b).³³ In both charge and discharge processes, the $\text{S}/\text{Cu}_{1.8}\text{Se}$ electrode exhibited lower overpotentials than $\text{S}/\text{Cu}_2\text{Se}$ and $\text{S}/\text{Super P}$ electrodes, indicating a promoted Li-S reaction.

The galvanostatic charge/discharge profiles of $\text{S}/\text{Cu}_{1.8}\text{Se}$, $\text{S}/\text{Cu}_2\text{Se}$, and $\text{S}/\text{Super P}$ electrodes at various current densities, from 0.1 to 5 C are displayed in Figure 5c and Figure S14. Figure 5d compares the rate performances of the three types of electrodes tested. Copper selenide electrodes displayed significantly higher capacities than carbon black. The $\text{S}/\text{Cu}_{1.8}\text{Se}$ electrode showed the largest capacity among the different electrodes tested, with two clear discharge plateaus at all current rates. The $\text{S}/\text{Cu}_{1.8}\text{Se}$ electrode displayed the best rate capability with a high capacity of 1218 mAh g^{-1} at 0.2 C and 588 mAh g^{-1} at 5 C. When switched back to 0.2 C, the capacity recovered to 1148 mAh g^{-1} , corresponding to 94.3% of its initial value, indicating remarkable electrochemical reversibility. In comparison, the cells based on $\text{S}/\text{Super P}$ undergo rapid capacity fading when increasing the current rate to 5 C. The excellent rate capability of the copper selenides, especially the $\text{S}/\text{Cu}_{1.8}\text{Se}$ electrode, is consistent with their high ability to accelerate the charge transfer and promote the conversion of polysulfides.

The energy conversion efficiency of the cells in the charge/discharge process was calculated by the ratio of energy output/input ($E = \int UIdt$).^{35,52} At 0.1 C current rate, the three types of electrode tested exhibited a high energy efficiency of around 90% (Figure 5e). When increasing the current rate, $\text{S}/\text{Cu}_{1.8}\text{Se}$ displayed the highest and most stable energy efficiency, with 88.5% efficiency at 1 C and 82.8% at 5 C. In contrast, the $\text{S}/\text{Super P}$ electrode was characterized with

just a 71.3% efficiency at 1 C. The high energy efficiency of the cathodes based on copper selenides, and particularly the S/Cu_{1.8}Se electrode, is associated with their low polarization potential and excellent catalytic activity.

Figure 5f displays the galvanostatic cycling performances of coin cells with different cathodes. Consistent with previous results, the S/Cu_{1.8}Se electrode enabled a remarkable initial capacity of 882 mAh g⁻¹ at 1C and 837 mAh g⁻¹ after 200 cycles, which corresponds to an outstanding capacity retention of 94.9 %. The S/Cu₂Se electrode also showed a notable initial capacity (770 mAh g⁻¹) and decent capacity retention of *ca.* 80% after 200 cycles. In contrast, the S/Super P electrode showed a moderate initial capacity (375 mAh g⁻¹) and low capacity retention (52.8%) after 200 cycles.

Figure 5g and Figure S15 display the Nyquist plot of the electrochemical impedance spectroscopy (EIS) data obtained from S/Cu_{1.8}Se, S/Cu₂Se, and S/Super P coin cells before and after cycling at 1 C. For the fresh electrodes, the semicircle in the high-frequency region is related to the charge-transfer resistance (R_{ct}), and the linear feature in the low-frequency region is associated with the diffusion of lithium ions.^{48,53} Based on the equivalent circuit shown in Figure S15c, a relatively low R_{ct} was obtained for the S/Cu_{1.8}Se electrodes (39.5 Ω), well below that of S/Cu₂Se (71.3 Ω) and S/Super P (87.8 Ω). After 200 charge/discharge cycles at 1C, an additional semicircle in the high-frequency range was evidenced. This new feature is associated with the resistance of an insoluble Li₂S₂/Li₂S passivation layer (R_p in the equivalent circuit shown in Figure S15d) grown during cycling.⁵³ After cycling, the S/Cu_{1.8}Se electrodes were characterized by smaller R_{ct} (9.8 Ω) and R_p (16.1 Ω), than S/Cu₂Se (R_{ct} =32.5 Ω , R_p =22.9 Ω) and S/Super P (R_{ct} =53.5 Ω , R_p =109 Ω) (Figure S16). This result confirms the important role

played by copper selenides and particularly $\text{Cu}_{1.8}\text{Se}$ in accelerating the LiPS conversion reaction and facilitating the charge transfer kinetics during lithiation/delithiation reactions.

Figure 5h displays the long term cycling performance of the electrodes at 3C. Copper selenide electrodes displayed an excellent cycling performance at this relatively high current rate, well above that of the cell based on a carbon cathode. Among the two copper selenides tested, the highly defective cubic $\text{Cu}_{1.8}\text{Se}$ showed the best cyclability, retaining a high reversible capacity of 527 mAh g^{-1} after 1000 cycles at 3 C, which corresponds to a tiny capacity fading rate of 0.029% per cycle. The outstanding capacity, rate capability and cyclability of the $\text{Cu}_{1.8}\text{Se}$ cathodes are attributed to the highly conductive nature, rapid ion transfer, excellent catalytic activity, and good LiPS affinity of this material, which immobilizes LiPS species and effectively accelerate their electrochemical conversion.

A key step toward the real-world application of LSBs is increasing the sulfur loading to rise the energy density of the overall device. Thus, the performance of S/ $\text{Cu}_{1.8}\text{Se}$ cathodes with higher sulfur loadings of 3.2, 5.1, and 7.2 mg cm^{-2} was also evaluated. As shown in Figure 6a, at a 0.1C current rate, two-plateau voltage profile is discerned under high the highest sulfur loadings tested, up to 7.2 mg cm^{-2} , with a high areal capacity of 6.07 mAh cm^{-2} , that largely exceeds the industrially requested areal capacity of LIBs ($\sim 4 \text{ mAh cm}^{-2}$). S/ $\text{Cu}_{1.8}\text{Se}$ -based cells containing high sulphur loads also demonstrated a notable rate performance (Figure 6b), achieving areal capacities of 3.01, 4.54, and 5.40 mAh cm^{-2} at 0.2 C when containing 3.2, 5.1, and 7.2 mg cm^{-2} of sulfur, respectively. As shown in Figure 6c, the high sulfur loaded Li-S cells based on S/ $\text{Cu}_{1.8}\text{Se}$ cathodes also showed a notably stable Li-S electrochemistry, with just a slight potential hysteresis after 50 cycles that indicates a minor LiPS shuttling. Figure 6d displays the

1
2
3
4 cycling performances of the high sulphur loaded cells. S/Cu_{1.8}Se cathodes showed high capacity
5
6 retention after 100 cycles, with areal capacities of 3.32, 4.27, and 5.00 mAh cm⁻² at sulfur
7
8 loadings of 3.2, 5.1, and 7.2 mg cm⁻², respectively.
9
10

11 As a practical demonstration of the potential of LSB cells based on Cu_{1.8}Se cathodes, an electric
12
13 fan with a light pattern was powered with a single coin cell (Figure 6e). Besides, the excellent
14
15 performance of Cu_{1.8}Se-based cathodes is placed in context in Figure 6f and Table S1, where
16
17 results obtained in the present work are compared with those reported in previous publications.
18
19
20
21
22
23
24

25 CONCLUSIONS

26
27 In summary, we demonstrated copper selenides produced by a facile solution-based method to
28
29 be an efficient multifunctional sulphur host material in LSB cathodes. Both experimental results
30
31 and computational data demonstrated the excellent electrochemical performance of copper
32
33 selenides, and particularly Cu_{1.8}Se, to be attributed to: i) The presence of a combination of
34
35 lithiophilic/sulfiphilic sites which contributes to an effective trapping of LiPS and the related
36
37 promotion of the Li⁺ diffusion; ii) high electrical conductivity of Cu_{1.8}Se associated to its high
38
39 density of copper vacancies; and iii) A large improvement of the Li-S reaction kinetics during
40
41 the battery charge/discharge processes, including LiPS phase change and Li₂S
42
43 deposition/dissolution. Among the copper selenides tested, experimental data and DFT
44
45 calculations pointed at the defective cubic Cu_{1.8}Se structure as the most effective to trap LiPS
46
47 and to catalytically accelerate the Li-S reversible reaction. Attributed to these beneficial
48
49 features, S/Cu_{1.8}Se cathodes delivered excellent long-term cycling stability with a low capacity
50
51 fading of 0.029% per cycle over 1000 cycles, a remarkable rate capability up to 5 C, and a high
52
53
54
55
56
57
58
59
60

areal capacity of 6.07 mAh cm⁻² under a high sulfur load (7.2 mg cm⁻²). This work demonstrates that multifunctional sulphur hosts, with high adsorption and catalytic capabilities for rapid LPS adsorption-conversion process, hold a great promise in promoting the practical application of LSBs.

EXPERIMENTAL SECTION

Chemicals: Copper(II) chloride dihydrate (CuCl₂·2H₂O, 99+%), selenium pieces (99.999%), and 1-octadecene (ODE, technical grade 90%) were purchased from Aldrich. Trioctylphosphine (TOP, 97%) was purchased from Strem Chemicals. Oleylamine (OAm, C18 content approximately 80-90%) was purchased from Fisher. Analytical grade ethanol and hexane were obtained from various sources. All chemicals were used as received, without further purification. A stock solution of TOPSe (1 M) was prepared by dissolving 0.789 g of selenium pieces in 10 mL of TOP. All syntheses were carried out using standard vacuum/argon Schlenk lines.

Synthesis of Cu_{1.8}Se and Cu₂Se: In a typical synthesis, 9 mmol of CuCl₂·2H₂O was mixed with 30 mL of ODE and 70 mL of OAm in a 250 mL three-neck flask. The mixture was degassed under vacuum for 20 min at room temperature and then heated to 120 °C for 1h under vacuum. Afterwards, the solution was flushed with Ar and heated up to 220 °C. At this temperature, 5 mL of the TOP-Se stock solution was quickly injected. After injection, the reaction temperature was maintained at 220 °C for 20 min. Then, the solution was cooled using a water bath. Cu_{1.8}Se nanoparticles (NPs) were precipitated and redispersed several times using ethanol and hexane. Then, Cu_{1.8}Se NPs were dried under vacuum and kept in an Ar-filled

glovebox until their posterior use. Cu₂Se was obtained by annealing the Cu_{1.8}Se NPs under a reducing atmosphere (5% H₂ in Ar) at 600°C for 3h.

Synthesis of S/Cu_{1.8}Se, S/Cu₂Se and S/Super P: Typically, Cu_{1.8}Se and sulfur powder were mixed with a weight ratio of 1:3, and then the mixture was heated at 155 °C for 8 h in a sealed glass bottle under Ar protection. Then the powder was immersed in a 10 mL CS₂ and ethanol solution (1:4, volume ratio) several times to remove the redundant sulfur not incorporated into Cu_{1.8}Se. S/Cu₂Se and S@Super P were prepared by the same method.

Materials Characterization: X-ray diffraction (XRD) patterns were obtained using a Bruker AXS D8 Advance X-ray diffractometer with Cu K radiation ($\lambda = 1.5106 \text{ \AA}$) operating at 40 kV and 40 mA. The morphology and microstructure of samples were characterized in a ZEISS Auriga Field emission scanning electron microscopy (FESEM) equipped with an energy-dispersive X-ray spectroscopy (EDS) detector operated at 20 kV. Transmission electron microscopy (TEM) characterization was carried out on a Zeiss Libra 120 (Carl Zeiss, Jena, Germany) operating at 120 kV. High-resolution TEM (HRTEM) and scanning TEM (STEM) were measured using a field emission gun FEI Tecnai F20 microscope at 200 kV. High angle annular dark-field (HAADF) STEM was combined with electron energy loss spectroscopy (EELS) in the Tecnai microscope by using a GATAN QUANTUM filter. X-ray photoelectron spectroscopy (XPS) measurements were performed using an Al anode XR50 source operating at 150 mW and a Phoibos 150 MCD-9 detector. Thermogravimetric (TGA) (PerkinElmer Diamond TG/DTA instrument.) experiment was carried out to record the ratio of S within the prepared composites. UV-vis absorption spectra were identified by the PerkinElmer LAMBDA 950 UV-vis spectrophotometer. Nitrogen adsorption-desorption isotherms were recorded to

calculate the specific surface area and analysis of the pore size distribution by Brunauer-Emmett-Teller method (Tristar II 3020 Micromeritics system).

Electrochemical Measurements: LSB performance was tested at room temperature in CR2032 coin-type cells. Active materials (S/Cu_{1.8}Se, S/Cu₂Se and S/Super P), PVDF binders and Super P were mixed (weight ratio = 8:1:1) in NMP to form a black slurry and then coated on Al foils and dried at 60 °C overnight. The prepared homogeneous slurry was coated on an aluminium foil and vacuum dried at 60 °C overnight. Subsequently, the coated aluminium foil was punched into small disks with a diameter of 12.0 mm as the cathode. Sulfur loading was about 1.0 mg cm⁻² (E/S = 20 μL mg⁻¹). Lithium foils were used as anode and Celgard 2400 membranes as separators. The electrolyte was prepared by dissolving 1.0 M lithium bis(trifluoromethanesulfonyl)imide in a mixture of DOL and DME (v/v = 1/1) with 0.2 M LiNO₃ additive. Galvanostatic charge-discharge (GCD) tests were performed on a Neware BTS4008 battery tester with different C rates. Cyclic voltammetry (CV) measurements were performed on a battery tester BCS-810 from Bio Logic at a scan rate of 0.1-0.4 mV s⁻¹ with an electrochemical window of 1.7-2.8 V, and electrochemical impedance spectroscopy (EIS) tests with a voltage amplitude of 10 mV in the frequency range 100 kHz to 0.01 Hz were performed.

Preparation of Li₂S₄ solutions for adsorption test: Sulfur and Li₂S with a molar ratio of 3:1 were dissolved into a certain amount of DME and DOL (volume ratio of 1:1) for continuous stirring overnight in a glove box, which eventually yielded a homogeneous dark brown solution. To evaluate the polysulfide absorption ability, 15 mg of Cu_{1.8}Se, Cu₂Se and Super P were poured into 3.0 mL 10 mM Li₂S₄ solution, respectively. The obtained mixtures were vigorously stirred for 2 h and aged overnight under Ar atmosphere.

Symmetric Cell Assembly and Measurements: Symmetric cells were assembled and tested using the same process as for LSBs. Two pieces of the same electrode (average S loading about 0.5 mg cm^{-2}) were used as identical working and counter electrodes. Each coin cell contained 40 μL of electrolyte (0.5 M Li_2S_6 and 1 M LiTFSI in 1:1 DOL/DME (v/v)). CV measurements were carried out at a scan rate of 20 mV s^{-1} .

Measurement of Nucleation of Li_2S : Standard 2032 coin cells were assembled to analyze the nucleation of Li_2S . A certain amount of host materials ($\text{Cu}_{1.8}\text{Se}$ and Cu_2Se) were dissolved in ethanol. Then the catalysts were coated on the carbon papers applied as the working electrode. Li foil worked as the counter electrode. The catholyte consisted of 20 μL of 0.25 M Li_2S_8 dissolved in tetraglyme with 1.0 M LiTFSI. The anolyte contained 20 μL of 1.0 M LiTFSI in tetraglyme solution without Li_2S_8 . The cells were first discharged at a current of 0.112 mA to 2.06 V and then hold the voltage at 2.05 V until the current decreased to 0.01 mA for Li_2S nucleation and growth.

Supporting Information

The supporting information is available free of charge via the Internet at <http://pubs.acs.org>.

The supporting information includes Figure S1-S16 and Table S1 as described in the text, specifically, additional SEM, TEM, XRD, TGA, CV, electrochemical performance, DFT simulation results, and crystal structure.

Corresponding Author

Email: limengyao@irec.cat

Email: wangjiaao0720@utexas.edu

Email: david.mitlin2@utexas.edu

Email: chou@wzu.edu.cn

Email: acabot@irec.cat

ACKNOWLEDGMENTS

The authors thank support from the projects ENE2016-77798-C4-3-R and NANOGEN (PID2020-116093RB-C43), funded by MCIN/ AEI/10.13039/501100011033/ and by “ERDF A way of making Europe”, by the “European Union”. D. Yang, M. Li, X. Han and C. Zhang thank the China Scholarship Council for the scholarship support. ICN2 acknowledges the support from the Severo Ochoa Programme (MINECO, grant no. SEV-2017-0706). IREC and ICN2 are both funded by the CERCA Program/Generalitat de Catalunya. This project has received funding from the European Union’s Horizon 2020 research and innovation program under grant agreement No 823717 – ESTEEM3. Calculations at UT Austin were supported by the Welch Foundation (F-1841) and the Texas Advanced Computing Center. Part of the present work has been performed in the framework of Universitat Autònoma de Barcelona Materials Science PhD program. J. Llorca is a Serra Hünter Fellow and is grateful to MICINN/FEDER RTI2018-093996-B-C31, GC 2017 SGR 128 and to ICREA Academia program.

REFERENCES

- (1) Bai, S.; Liu, X.; Zhu, K.; Wu, S.; Zhou, H. Metal-Organic Framework-Based Separator for Lithium-Sulfur Batteries. *Nat. Energy* **2016**, *1*, 16049.
- (2) Chou, S.; Dou, S. Next-Generation Batteries. *Adv. Mater.* **2017**, *29*, 1–3.
- (3) Seh, Z. W.; Sun, Y.; Zhang, Q.; Cui, Y. Designing High-Energy Lithium-Sulfur Batteries. *Chem. Soc. Rev.* **2016**, *45*, 5605–5634.

- (4) Bruce, P. G.; Freunberger, S. A.; Hardwick, L. J.; Tarascon, J. M. LiO₂ and LiS Batteries with High Energy Storage. *Nat. Mater.* **2012**, *11*, 19–29.
- (5) Manthiram, A.; Fu, Y.; Chung, S. H.; Zu, C.; Su, Y. S. Rechargeable Lithium-Sulfur Batteries. *Chem. Rev.* **2014**, *114*, 11751–11787.
- (6) Li, Z.; Wu, H. Bin; Lou, X. W. Rational Designs and Engineering of Hollow Micro-/Nanostructures as Sulfur Hosts for Advanced Lithium-Sulfur Batteries. *Energy Environ. Sci.* **2016**, *9*, 3061–3070.
- (7) Liang, X.; Rangom, Y.; Kwok, C. Y.; Pang, Q.; Nazar, L. F. Interwoven MXene Nanosheet/Carbon-Nanotube Composites as Li–S Cathode Hosts. *Adv. Mater.* **2017**, *29*, 1603040.
- (8) Xu, F.; Tang, Z.; Huang, S.; Chen, L.; Liang, Y.; Mai, W.; Zhong, H.; Fu, R.; Wu, D. Facile Synthesis of Ultrahigh-Surface-Area Hollow Carbon Nanospheres for Enhanced Adsorption and Energy Storage. *Nat. Commun.* **2015**, *6* (7221).
- (9) Du, Z.; Chen, X.; Hu, W.; Chuang, C.; Xie, S.; Hu, A.; Yan, W.; Kong, X.; Wu, X.; Ji, H.; Wan, L. J. Cobalt in Nitrogen-Doped Graphene as Single-Atom Catalyst for High-Sulfur Content Lithium-Sulfur Batteries. *J. Am. Chem. Soc.* **2019**, *141*, 3977–3985.
- (10) Schuster, J.; He, G.; Mandlmeier, B.; Yim, T.; Lee, K. T.; Bein, T.; Nazar, L. F. Spherical Ordered Mesoporous Carbon Nanoparticles with High Porosity for Lithium-Sulfur Batteries. *Angew. Chemie-Int. Ed.* **2012**, *51*, 3591–3595.
- (11) Wang, X.; Li, G.; Li, J.; Zhang, Y.; Wook, A.; Yu, A.; Chen, Z. Structural and Chemical Synergistic Encapsulation of Polysulfides Enables Ultralong-Life Lithium-Sulfur Batteries. *Energy Environ. Sci.* **2016**, *9*, 2533–2538.
- (12) Liang, X.; Hart, C.; Pang, Q.; Garsuch, A.; Weiss, T.; Nazar, L. F. A Highly Efficient Polysulfide Mediator for Lithium–Sulfur Batteries. *Nat. Commun.* **2015**, *6* (5682).
- (13) Cui, Z.; Zu, C.; Zhou, W.; Manthiram, A.; Goodenough, J. B. Mesoporous Titanium Nitride-Enabled Highly Stable Lithium-Sulfur Batteries. *Adv. Mater.* **2016**, *28*, 6926–6931.

- (14) Zhong, Y.; Yin, L.; He, P.; Liu, W.; Wu, Z.; Wang, H. Surface Chemistry in Cobalt Phosphide-Stabilized Lithium-Sulfur Batteries. *J. Am. Chem. Soc.* **2018**, *140*, 1455–1459.
- (15) Wang, J.; Zhao, Y.; Li, G.; Luo, D.; Liu, J.; Zhang, Y.; Wang, X.; Shui, L.; Chen, Z. Aligned Sulfur-Deficient ZnS_{1-x} Nanotube Arrays as Efficient Catalyzer for High-Performance Lithium/Sulfur Batteries. *Nano Energy* **2021**, *84*, 105891.
- (16) Lin, H.; Yang, L.; Jiang, X.; Li, G.; Zhang, T.; Yao, Q.; zheng, wesley, G.; Lee, jim yang. Electrocatalysis of Polysulfide Conversion by Sulfur-Deficient MoS_2 Nanoflakes for Lithium-Sulfur Batteries. *Energy Environ. Sci.* **2017**, *10*, 1476–1486.
- (17) Lei, T.; Chen, W.; Huang, J.; Yan, C.; Sun, H.; Wang, C.; Zhang, W.; Li, Y.; Xiong, J. Multi-Functional Layered WS_2 Nanosheets for Enhancing the Performance of Lithium–Sulfur Batteries. *Adv. Energy Mater.* **2017**, *7*, 1–8.
- (18) Wang, Y.; Yang, D.; Lian, J.; Wei, T.; Sun, Y. Ordered Corn-like CuCo_2O_4 Nanoforests Covering Ni Foam for a High-Performance All-Solid-State Supercapacitor. *J. Alloys Compd.* **2018**, *741*, 527–531.
- (19) Xin, X.; Song, Y.; Guo, S.; Zhang, Y.; Wang, B.; Yu, J.; Li, X. In-Situ Growth of High-Content 1T Phase MoS_2 Confined in the CuS Nanoframe for Efficient Photocatalytic Hydrogen Evolution. *Appl. Catal. B Environ.* **2020**, *269*, 118773.
- (20) Li, M.; Liu, Y.; Zhang, Y.; Han, X.; Zhang, T.; Zuo, Y.; Xie, C.; Xiao, K.; Arbiol, J.; Llorca, J.; Ibáñez, M.; Liu, J.; Cabot, A. Effect of the Annealing Atmosphere on Crystal Phase and Thermoelectric Properties of Copper Sulfide. *ACS Nano* **2021**, *15*, 4967–4978.
- (21) Coughlan, C.; Ibáñez, M.; Dobrozhana, O.; Singh, A.; Cabot, A.; Ryan, K. M. Compound Copper Chalcogenide Nanocrystals. *Chem. Rev.* **2017**, *117*, 5865–6109.
- (22) Chen, H.; Fang, C.; Gao, X.; Jiang, G.; Wang, X.; Sun, S. P.; Duo Wu, W.; Wu, Z. Sintering- and Oxidation-Resistant Ultrasmall Cu(I)/(II) Oxides Supported on Defect-Rich Mesoporous Alumina Microspheres Boosting Catalytic Ozonation. *J. Colloid Interface Sci.* **2021**, *581*, 964–978.
- (23) Yang, D.; Zhu, Q.; Chen, C.; Liu, H.; Liu, Z.; Zhao, Z.; Zhang, X.; Liu, S.; Han, B.

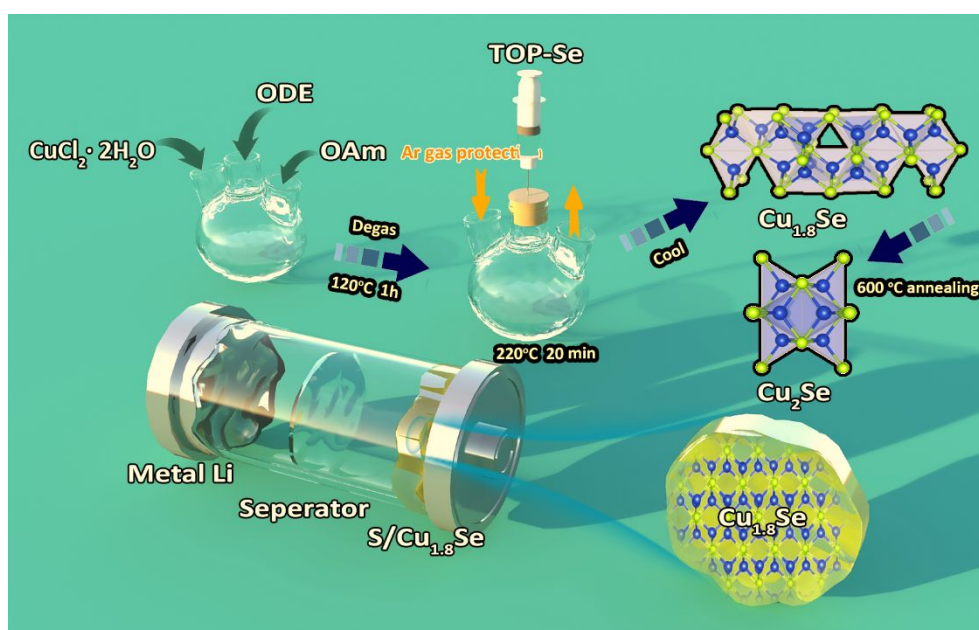
- Selective Electroreduction of Carbon Dioxide to Methanol on Copper Selenide Nanocatalysts. *Nat. Commun.* **2019**, *10*, 1–9.
- (24) Chen, H.; Gao, Y.; Ye, L.; Yao, Y.; Chen, X.; Wei, Y.; Sun, L. A Cu₂Se-Cu₂O Film Electrodeposited on Titanium Foil as a Highly Active and Stable Electrocatalyst for the Oxygen Evolution Reaction. *Chem. Commun.* **2018**, *54*, 4979–4982.
- (25) Yu, Q.; Lu, Y.; Luo, R.; Liu, X.; Huo, K.; Kim, J. K.; He, J.; Luo, Y. In Situ Formation of Copper-Based Hosts Embedded within 3D N-Doped Hierarchically Porous Carbon Networks for Ultralong Cycle Lithium–Sulfur Batteries. *Adv. Funct. Mater.* **2018**, *28*, 1–12.
- (26) Sun, K.; Su, D.; Zhang, Q.; Bock, D. C.; Marschilok, A. C.; Takeuchi, K. J.; Takeuchi, E. S.; Gan, H. Interaction of CuS and Sulfur in Li-S Battery System. *J. Electrochem. Soc.* **2015**, *162*, A2834–A2839.
- (27) Hosseini, S. M.; Varzi, A.; Ito, S.; Aihara, Y.; Passerini, S. High Loading CuS-Based Cathodes for All-Solid-State Lithium Sulfur Batteries with Enhanced Volumetric Capacity. *Energy Storage Mater.* **2020**, *27*, 61–68.
- (28) He, D.; Xue, P.; Song, D.; Qu, J.; Lai, C. Tri-Functional Copper Sulfide as Sulfur Carrier for High-Performance Lithium-Sulfur Batteries. *J. Electrochem. Soc.* **2017**, *164*, A1499–A1502.
- (29) Li, X.; Lv, W.; Wu, G.; Fu, G.; Zhang, W.; Li, Z. A Novel CuSe-Cu_{1.8}Se Heterostructure with Hexahedral Structure Cathode Material for Aluminum Batteries. *Chem. Eng. J.* **2021**, *426*, 131899.
- (30) Gao, F.; Zhu, L.; Wang, Y.; Xie, H.; Li, J. Room Temperature Facile Synthesis of Cu₂Se Hexagonal Nanoplates Array Film and Its High Photodegradation Activity to Methyl Blue with the Assistance of H₂O₂. *Mater. Lett.* **2016**, *183*, 425–428.
- (31) Li, W.; Ma, Y.; Li, P.; Jing, X.; Jiang, K.; Wang, D. Electrochemically Activated Cu_{2-x}Te as an Ultraflat Discharge Plateau, Low Reaction Potential, and Stable Anode Material for Aqueous Zn-Ion Half and Full Batteries. *Adv. Energy Mater.* **2021**, *11*, 1–

- 11.
- (32) Zhang, D. M.; Jia, J. H.; Yang, C. C.; Jiang, Q. Fe₇Se₈ Nanoparticles Anchored on N-Doped Carbon Nanofibers as High-Rate Anode for Sodium-Ion Batteries. *Energy Storage Mater.* **2020**, *24*, 439–449.
- (33) Yang, D.; Liang, Z.; Zhang, C.; Biendicho, J. J.; Botifoll, M.; Spadaro, M. C.; Chen, Q.; Li, M.; Ramon, A.; Moghaddam, A. O.; Llorca, J.; Wang, J.; Morante, J. R.; Arbiol, J.; Chou, S. L.; Cabot, A. NbSe₂ Meets C₂N: A 2D-2D Heterostructure Catalysts as Multifunctional Polysulfide Mediator in Ultra-Long-Life Lithium–Sulfur Batteries. *Adv. Energy Mater.* **2021**, *11*, 2101250.
- (34) Guo, Q.; Li, S.; Liu, X.; Lu, H.; Chang, X.; Zhang, H.; Zhu, X.; Xia, Q.; Yan, C.; Xia, H. Ultrastable Sodium–Sulfur Batteries without Polysulfides Formation Using Slit Ultramicropore Carbon Carrier. *Adv. Sci.* **2020**, *7*, 1–12.
- (35) Yang, D.; Zhang, C.; Biendicho, J. J.; Han, X.; Liang, Z.; Du, R.; Li, M.; Li, J.; Arbiol, J.; Llorca, J.; Zhou, Y.; Morante, J. R.; Cabot, A. ZnSe/N-Doped Carbon Nanoreactor with Multiple Adsorption Sites for Stable Lithium-Sulfur Batteries. *ACS Nano* **2020**, *14*, 15492–15504.
- (36) Shi, H.; Qin, J.; Lu, P.; Dong, C.; He, J.; Chou, X.; Das, P.; Wang, J.; Zhang, L.; Wu, Z. S. Interfacial Engineering of Bifunctional Niobium (V)-Based Heterostructure Nanosheet Toward High Efficiency Lean-Electrolyte Lithium–Sulfur Full Batteries. *Adv. Funct. Mater.* **2021**, *31*, 1–10.
- (37) Luo, D.; Li, G.; Deng, Y. P.; Zhang, Z.; Li, J.; Liang, R.; Li, M.; Jiang, Y.; Zhang, W.; Liu, Y.; Lei, W.; Yu, A.; Chen, Z. Synergistic Engineering of Defects and Architecture in Binary Metal Chalcogenide toward Fast and Reliable Lithium–Sulfur Batteries. *Adv. Energy Mater.* **2019**, *9*, 1–10.
- (38) Cai, D.; Liu, B.; Zhu, D.; Chen, D.; Lu, M.; Cao, J.; Wang, Y.; Huang, W.; Shao, Y.; Tu, H.; Han, W. Ultrafine Co₃Se₄ Nanoparticles in Nitrogen-Doped 3D Carbon Matrix for High-Stable and Long-Cycle-Life Lithium Sulfur Batteries. *Adv. Energy Mater.* **2020**, *10*, 1904273.

- (39) Ci, H.; Cai, J.; Ma, H.; Shi, Z.; Cui, G.; Wang, M.; Jin, J.; Wei, N.; Lu, C.; Zhao, W.; Sun, J.; Liu, Z. Defective VSe₂-Graphene Heterostructures Enabling In Situ Electrocatalyst Evolution for Lithium-Sulfur Batteries. *ACS Nano* **2020**, *14*, 11929–11938.
- (40) Tian, Y.; Li, G.; Zhang, Y.; Luo, D.; Wang, X.; Zhao, Y.; Liu, H.; Ji, P.; Du, X.; Li, J.; Chen, Z. Low-Bandgap Se-Deficient Antimony Selenide as a Multifunctional Polysulfide Barrier toward High-Performance Lithium–Sulfur Batteries. *Adv. Mater.* **2020**, *32*, 1904876.
- (41) Jingwen, W.; Shoufu, C.; Likun, Y.; Yan, Z.; Kun, X.; Xiaoqing, L.; Jun, X. Metastable Marcasite NiSe₂ Nanodendrites on Carbon Fiber Clothes to Suppress Polysulfide Shuttling for High-Performance Lithium–Sulfur Batteries. *Nanoscale* **2021**, *13*, 16487–16498.
- (42) Liubin, W.; Youxuan, N.; Xuesen, H.; Li, C.; Fujun, L.; Jun, C. A Two-Dimensional Metal-Organic Polymer Enabled by Robust Nickel-Nitrogen and Hydrogen Bonds for Exceptional Sodium-Ion Storage. *Angew. Chemie - Int. Ed.* **2020**, *59*, 22126–22131.
- (43) Li, Y.; Wang, W.; Zhang, B.; Fu, L.; Wan, M.; Li, G.; Cai, Z.; Tu, S.; Duan, X.; Seh, Z. W.; Jiang, J.; Sun, Y. Manipulating Redox Kinetics of Sulfur Species Using Mott-Schottky Electrocatalysts for Advanced Lithium-Sulfur Batteries. *Nano Lett.* **2021**, *21*, 6656–6663.
- (44) Zhang, L.; Liu, D.; Muhammad, Z.; Wan, F.; Xie, W.; Wang, Y.; Song, L.; Niu, Z.; Chen, J. Single Nickel Atoms on Nitrogen-Doped Graphene Enabling Enhanced Kinetics of Lithium–Sulfur Batteries. *Adv. Mater.* **2019**, *31*, 1903955.
- (45) Xu, J.; Zhang, W.; Fan, H.; Cheng, F.; Su, D.; Wang, G. Promoting Lithium Polysulfide/Sulfide Redox Kinetics by the Catalyzing of Zinc Sulfide for High Performance Lithium-Sulfur Battery. *Nano Energy* **2018**, *51*, 73–82.
- (46) Song, Y.; Wen, Z.; Long, K.; Zhang, L.; Zhu, X.; Shao, Y.; Ding, F.; Zhang, Q.; Sun, J.; Liu, Z. Synchronous Immobilization and Conversion of Polysulfides on VO₂-VN Binary Host Targeting High Sulfur Loading Li-S Batteries. *Energy Environ. Sci.* **2018**, *11*, 28

- 2620–2630.
- (47) Liu, X.; He, Q.; Yuan, H.; Yan, C.; Zhao, Y.; Xu, X.; Huang, J. Q.; Chueh, Y. L.; Zhang, Q.; Mai, L. Interface Enhanced Well-Dispersed Co₉S₈ Nanocrystals as an Efficient Polysulfide Host in Lithium–Sulfur Batteries. *J. Energy Chem.* **2020**, *48*, 109–115.
- (48) Zhang, C.; Du, R.; Biendicho, J. J.; Yi, M.; Xiao, K.; Yang, D.; Zhang, T.; Wang, X.; Arbiol, J.; Llorca, J.; Zhou, Y.; Morante, J. R.; Cabot, A. Tubular CoFeP@CN as a Mott–Schottky Catalyst with Multiple Adsorption Sites for Robust Lithium–Sulfur Batteries. *Adv. Energy Mater.* **2021**, *11*, 1–14.
- (49) Zhao, H.; Tian, B.; Su, C.; Li, Y. Single-Atom Iron and Doped Sulfur Improve the Catalysis of Polysulfide Conversion for Obtaining High-Performance Lithium-Sulfur Batteries. *ACS Appl. Mater. Interfaces* **2021**, *13*, 7171–7177.
- (50) Cai, D.; Lu, M.; Li, L.; Cao, J.; Chen, D.; Tu, H.; Li, J.; Han, W. A Highly Conductive MOF of Graphene Analogue Ni₃(HITP)₂ as a Sulfur Host for High-Performance Lithium–Sulfur Batteries. *Small* **2019**, *15*, 1–11.
- (51) Zhifu, L.; Dawei, Y.; Pengyi, T.; Chaoqi, Z.; Jordi Jacas, B.; Yi, Z.; Jordi, L.; Xiang, W.; Junshan, L.; Marc, H.; Jeremy, D.; Rafal E, D.-B.; Yingtang, Z.; Joan Ramon, M.; Andreu, C.; Jordi, A. Atomically Dispersed Fe in a C₂N Based Catalyst as a Sulfur Host for Efficient Lithium–Sulfur Batteries. *Adv. Energy Mater.* **2021**, *11*, 2003507.
- (52) Eftekhari, A. Energy Efficiency: A Critically Important but Neglected Factor in Battery Research. *Sustain. Energy Fuels* **2017**, *1*, 2053–2060.
- (53) Shao, A. H.; Zhang, Z.; Xiong, D. G.; Yu, J.; Cai, J. X.; Yang, Z. Y. Facile Synthesis of a “Two-in-One” Sulfur Host Featuring Metallic-Cobalt-Embedded N-Doped Carbon Nanotubes for Efficient Lithium-Sulfur Batteries. *ACS Appl. Mater. Interfaces* **2020**, *12*, 5968–5978.
- (54) Baumann, A. E.; Aversa, G. E.; Roy, A.; Falk, M. L.; Bedford, N. M.; Thoi, V. S. Promoting Sulfur Adsorption Using Surface Cu Sites in Metal-Organic Frameworks for Lithium Sulfur Batteries. *J. Mater. Chem. A* **2018**, *6*, 4811–4821.

- (55) Geng, P.; Du, M.; Guo, X.; Pang, H.; Tian, Z.; Braunstein, P.; Xu, Q. Bimetallic Metal-Organic Framework with High-Adsorption Capacity toward Lithium Polysulfides for Lithium–Sulfur Batteries. *Energy Environ. Mater.* **2021**, *0*, 1–9.
- (56) Zhubing, X.; Zhi, Y.; Linjie, Z.; Hui, P.; Ruihu, W. Sandwich-Type NbS₂@S@I-Doped Graphene for High-Sulfur-Loaded, Ultrahigh-Rate and Long-Life Lithium-Sulfur Batteries. *ACS Nano* **2017**, *11*, 8488–8498.
- (57) Hao, Q.; Cui, G.; Zhang, Y.; Li, J.; Zhang, Z. Novel MoSe₂/MoO₂ Heterostructure as an Effective Sulfur Host for High-Performance Lithium/Sulfur Batteries. *Chem. Eng. J.* **2020**, *381*, 122672.



Scheme 1. Schematic illustration of the synthetic procedure used to produce copper selenide.

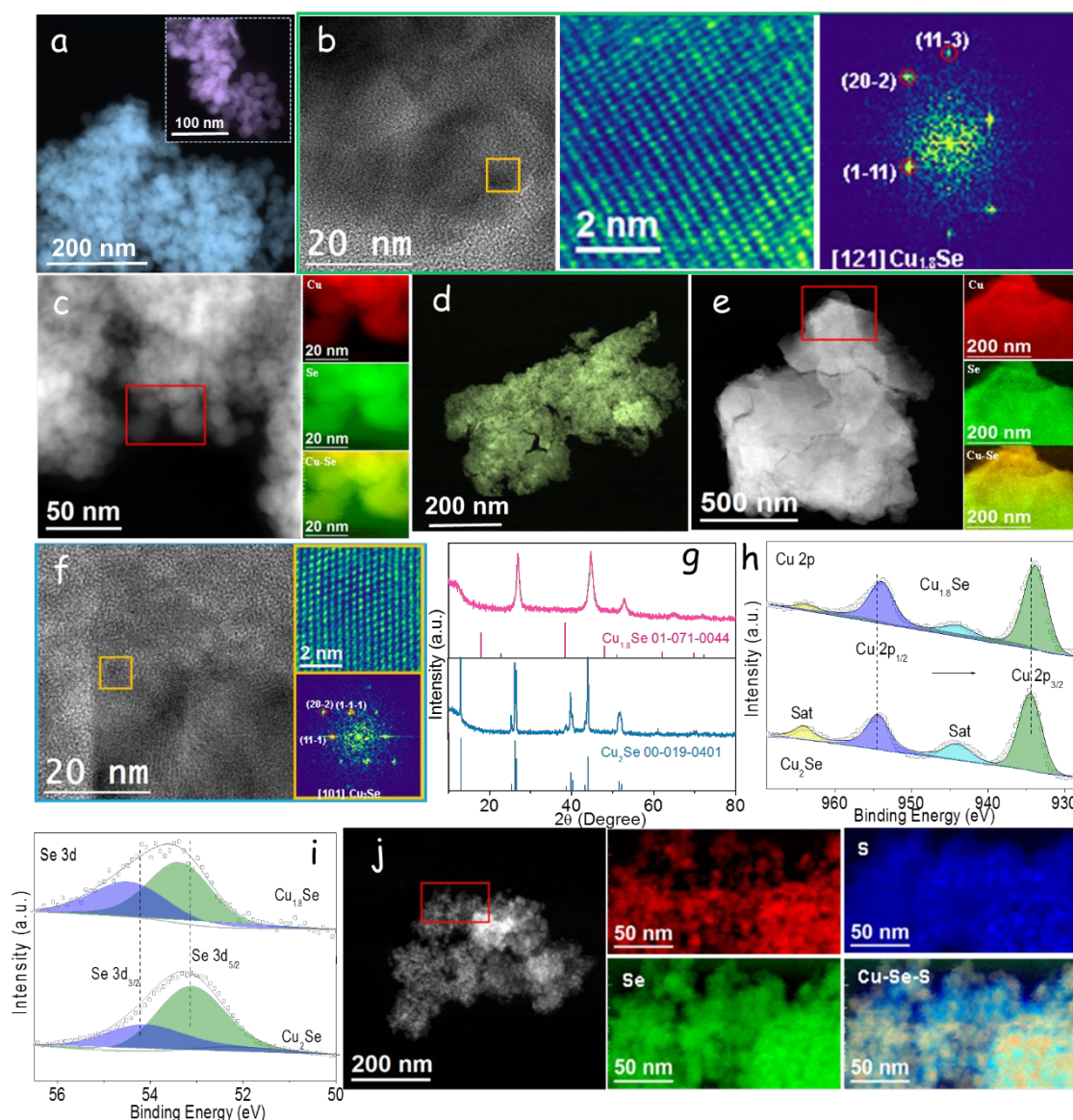


Figure 1. (a) TEM image of $\text{Cu}_{1.8}\text{Se}$. (b) HRTEM micrograph of $\text{Cu}_{1.8}\text{Se}$, detail of the orange squared region and its corresponding power spectrum. (c) EELS chemical composition maps obtained from the red squared area of the STEM micrograph of $\text{Cu}_{1.8}\text{Se}$. Individual Cu $L_{2,3}$ -edges at 931 eV (red) and Se $M_{1,2}$ -edges at 168 eV (green) and composites of Cu-Se. (d) TEM image of Cu_2Se . (e) EELS chemical composition maps obtained from the red squared area of the STEM micrograph of Cu_2Se . Individual Cu $L_{2,3}$ -edges at 931 eV (red) and Se $M_{1,2}$ -edges at 168 eV (green) and composites of Cu-Se. (f) HRTEM image of Cu_2Se and corresponding FFT spectrum of the enlarged image of the orange squared region. (g) XRD patterns of Cu_2Se and $\text{Cu}_{1.8}\text{Se}$. (h) Cu 2p high-resolution XPS spectra, and (i) Se 3d high-resolution XPS spectra from Cu_2Se and $\text{Cu}_{1.8}\text{Se}$. (j) EELS chemical composition maps obtained from the STEM micrograph

of a $\text{S}/\text{Cu}_{1.8}\text{Se}$ composite. Individual Cu $\text{L}_{2,3}$ -edges at 931 eV (red) and Se $\text{M}_{1,2}$ -edges at 168 eV (green), S $\text{L}_{2,3}$ -edge 165 eV (blue) and composites of Cu-Se-S.

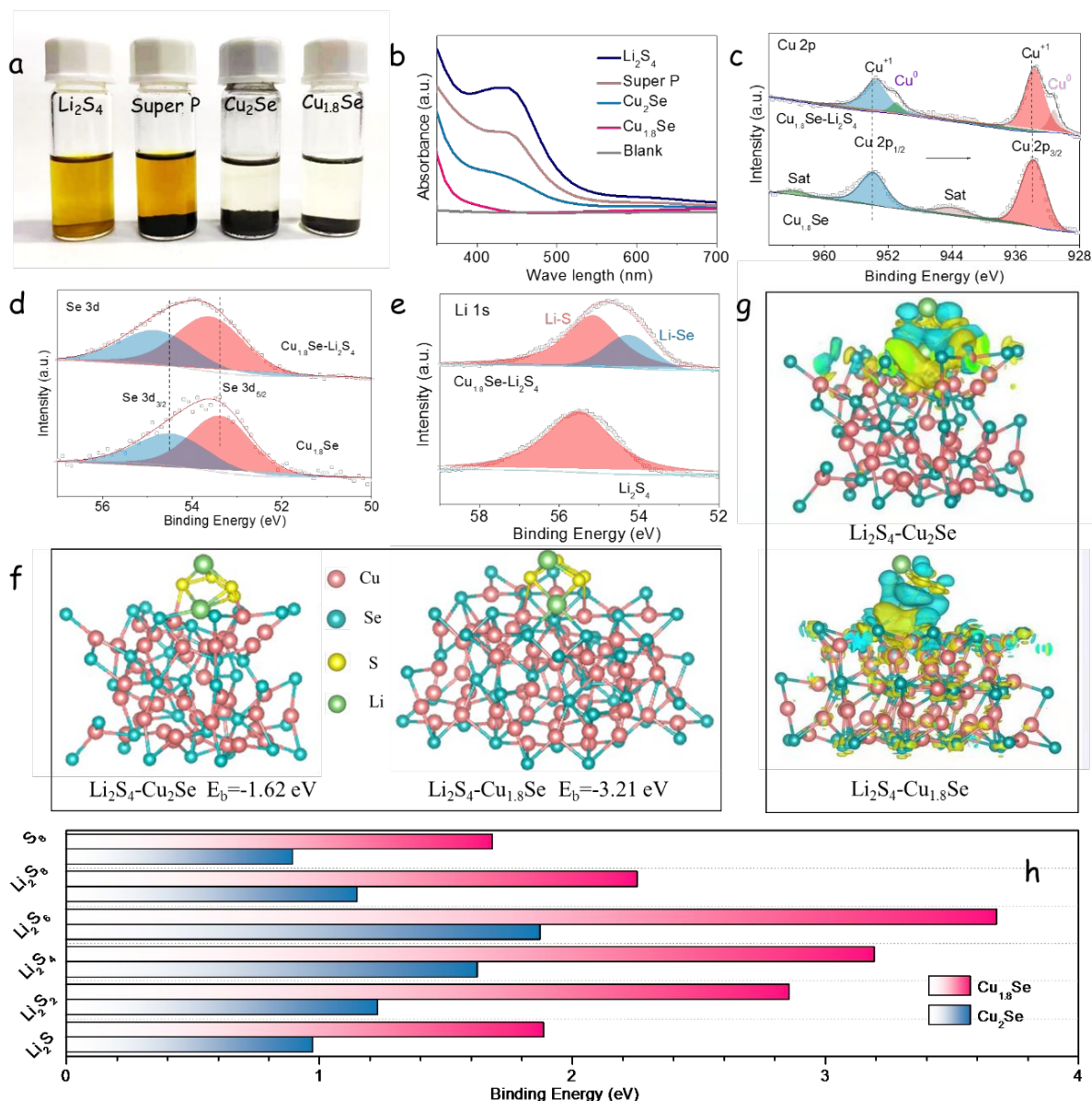


Figure 2. LiPS adsorption ability. (a) Optical image of $\text{Cu}_{1.8}\text{Se}$, Cu_2Se , and Super P materials soaked in Li_2S_4 solution after 12 h adsorption tests. (b) UV-vis spectrum of the absorbed Li_2S_4 solution containing the different adsorbents. (c-e) High-resolution XPS spectrum at (c) Cu 2p, (d) Se 3d, and (e) Li 1s core levels of the pristine $\text{Cu}_{1.8}\text{Se}$ and $\text{Cu}_{1.8}\text{Se}-\text{Li}_2\text{S}_4$, respectively. (f) Optimized adsorption configurations of LiPS species on the (220) facet of Cu_2Se and (111) facet of $\text{Cu}_{1.8}\text{Se}$, respectively. (g) Charge density difference of Li_2S_4 adsorbed on $\text{Cu}_{1.8}\text{Se}$ (111) and Cu_2Se (220). The yellow and cyan regions represent the accumulation and depletion of the

electron, respectively. (h) Binding energies of LiPS species (Li_2S , Li_2S_2 , Li_2S_4 , Li_2S_6 , Li_2S_8 and S_8) absorbed on $\text{Cu}_{1.8}\text{Se}$ and Cu_2Se surfaces, respectively, calculated with DFT.

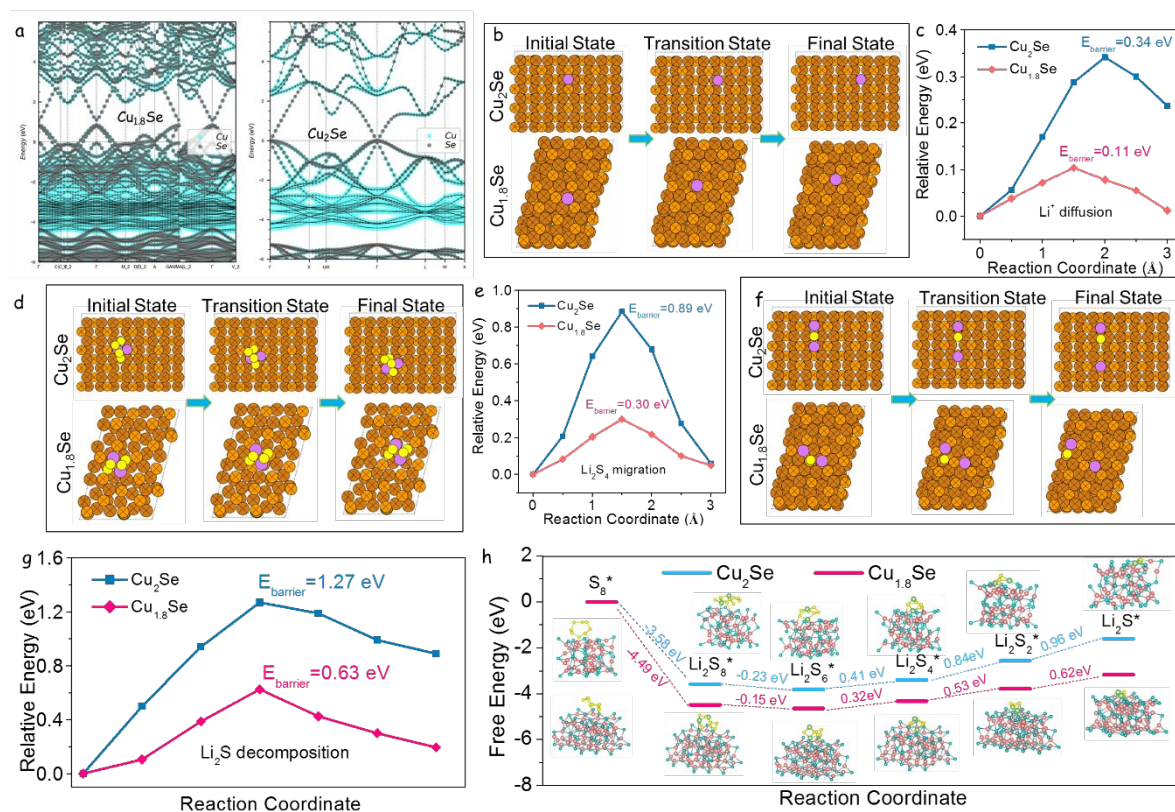


Figure 3. Lithium-ion diffusion and catalytic conversion kinetics studies of polysulfides in Li-S cells. (a) HSE06 band structures of Cu_2Se and $\text{Cu}_{1.8}\text{Se}$, respectively. (b) The total Li -ion diffusion paths on the optimized (220) facet of Cu_2Se and (111) facet of $\text{Cu}_{1.8}\text{Se}$, respectively. (c) Energy barrier of Li -ion diffusion on (220) facet of Cu_2Se and (111) facet of $\text{Cu}_{1.8}\text{Se}$, respectively. (d) Illustration of stages of Li_2S_4 diffusing on (002) facet of Cu_2Se and (111) facet of $\text{Cu}_{1.8}\text{Se}$, respectively. (e) Energy profiles of Li_2S_4 migration on (002) facet of Cu_2Se and (111) facet of $\text{Cu}_{1.8}\text{Se}$ along different adsorption sites. (f) Initial state, transition state and final state of Li_2S decomposition on (220) facet of Cu_2Se and (111) facet of $\text{Cu}_{1.8}\text{Se}$, respectively. (g) Energy barrier profiles of Li_2S cluster decomposition on Cu_2Se and $\text{Cu}_{1.8}\text{Se}$ along with different reaction coordinates. (h) Gibbs free energy profiles of LiPS species on Cu_2Se and $\text{Cu}_{1.8}\text{Se}$, showing a lower reaction free energy from Li_2S_2 to Li_2S on $\text{Cu}_{1.8}\text{Se}$ than that on Cu_2Se .

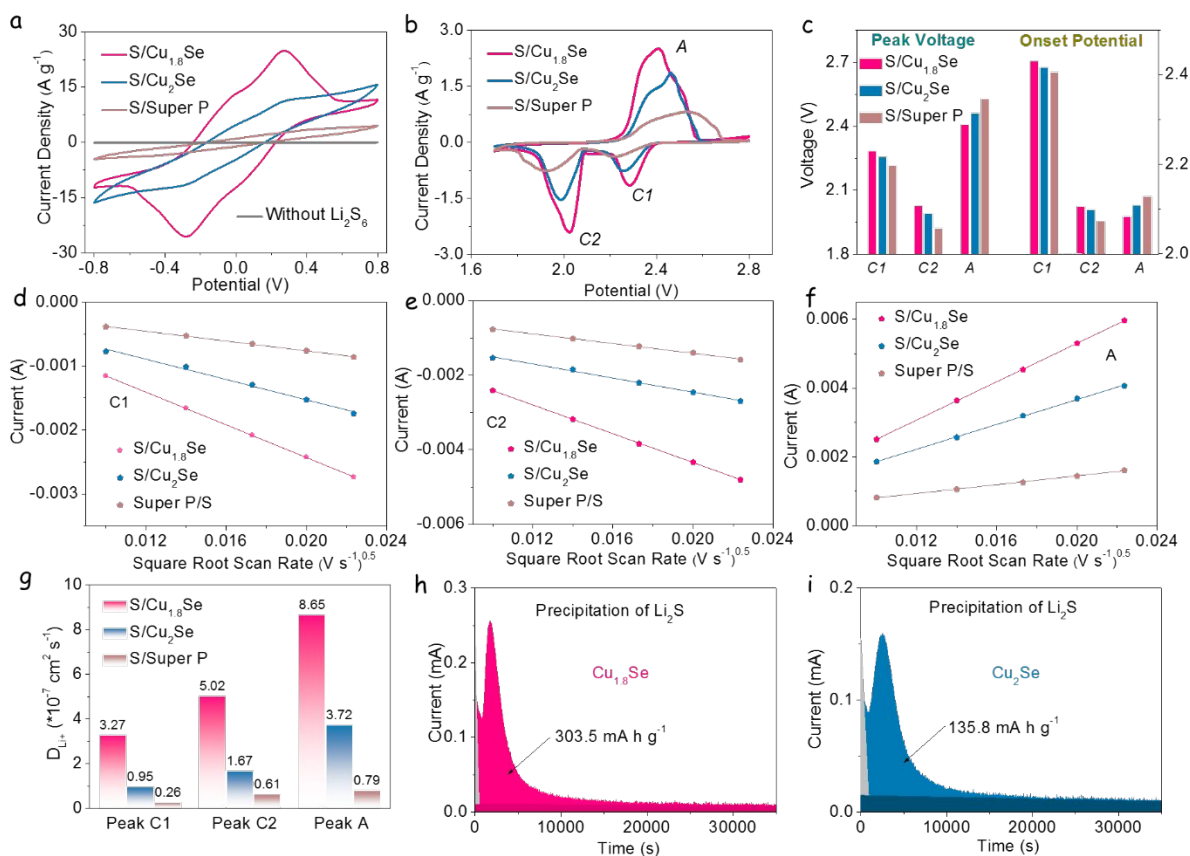


Figure 4. (a) CV profiles of symmetrical cells at a scan rate of 20 mV s⁻¹ with three different host materials using an electrolyte containing 0.5 mol L⁻¹ Li₂S₆ and 1 mol L⁻¹ LiTFSI dissolved in DOL/DME (v/v = 1/1). (b) CV profiles of Li-S coin cells with different electrodes. (c) Peak voltages and onset potentials obtained from CV curves of Li-S coin cells. (d-f) CV peak current values of peaks C1, C2, and A for S/Cu_{1.8}Se, S/Cu₂Se, and S/Super P electrodes versus the square root of scan rates. (g) Li⁺ diffusion coefficient value at peaks C1, C2, and A. (h,i) Potentiostatic discharge profile at 2.05 V with Li₂S₈ catholyte for evaluating the nucleation kinetics of Li₂S on Cu_{1.8}Se and Cu₂Se electrodes.

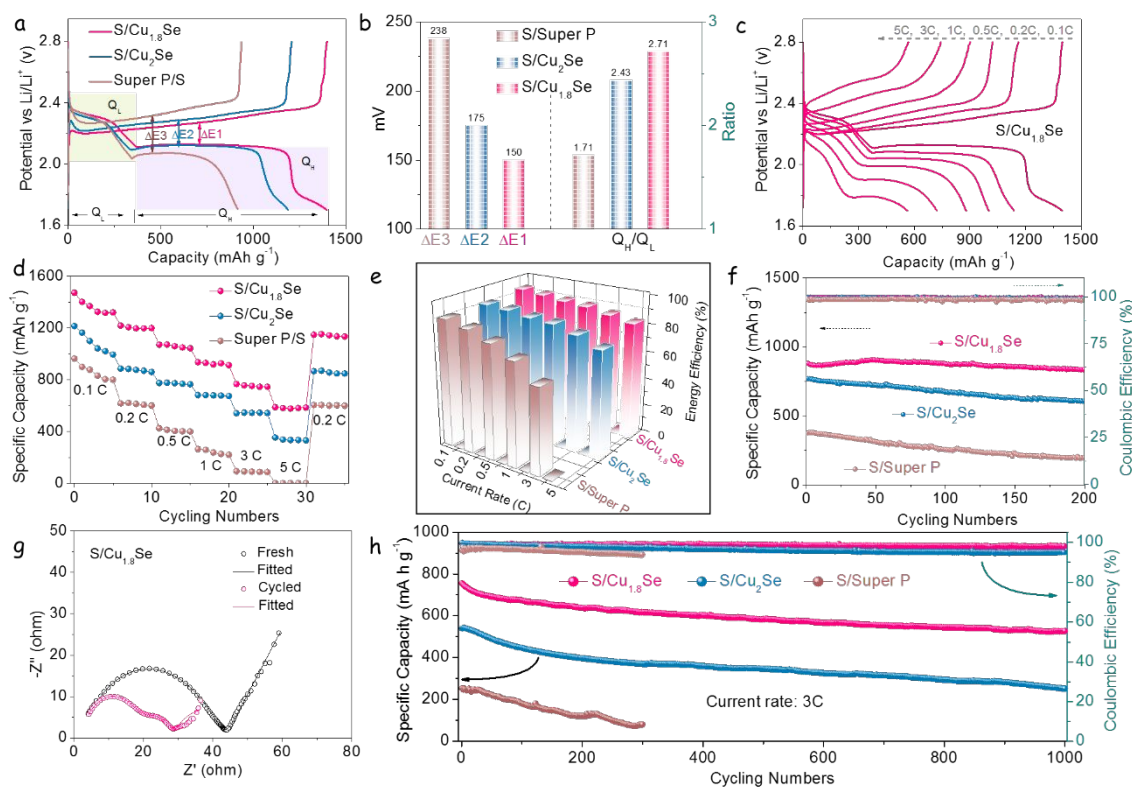


Figure 5. (a) Galvanostatic charge/discharge profiles of S/Cu_{1.8}Se, S/Cu₂Se, and S/Super P electrodes at a current rate of 0.1 C. (b) ΔE and Q_H/Q_L values obtained from charge/discharge curves. (c) Charge/discharge curves of the S/Cu_{1.8}Se electrodes at various C rates from 0.1 C to 5 C. (d) Rate capability of S/Cu_{1.8}Se, S/Cu₂Se, and S/Super P electrodes at various C rates from 0.1 C to 5 C. (e) Energy efficiencies of three different electrodes at different current densities. (f) Cycling performances of different electrodes at 1 C over 200 cycles. (g) EIS plot of S/Cu_{1.8}Se electrode before and after 200 cycles at 1 C. (h) Long-term cycling behaviour of Li-S cells based on S/Cu_{1.8}Se, S/Cu₂Se, and S/Super P electrodes at 3 C.

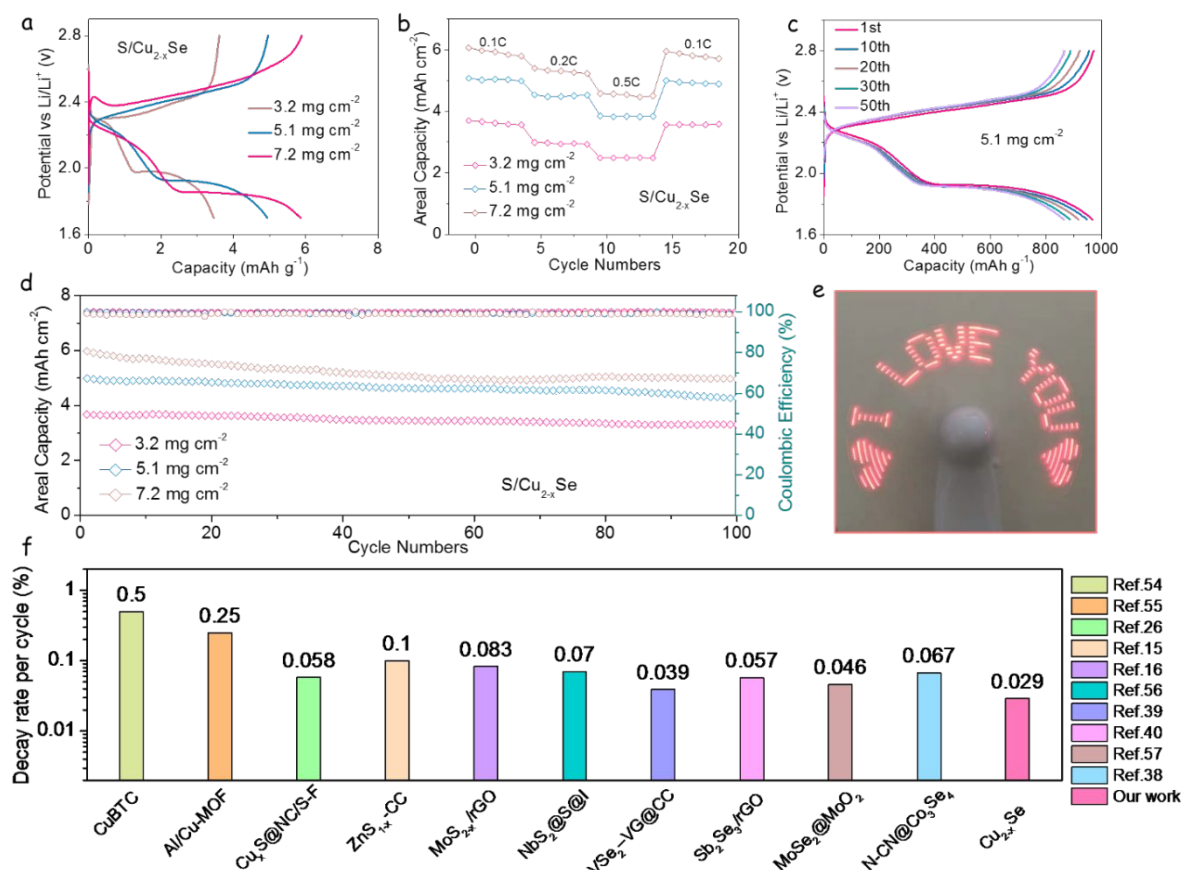


Figure 6. (a) Charge/discharge profiles at 0.1 C of S/Cu_{1.8}Se electrodes under raised sulfur loadings of 3.2, 5.1, and 7.2 mg cm⁻². (b) Rate capabilities with different sulfur loadings at various current densities. (c) Galvanostatic charge/discharge profiles at 0.1 C with a sulfur loading of 5.1 mg cm⁻². (d) High-loading cycling performances with sulfur loadings of 3.2, 5.1, and 7.2 mg cm⁻² at 0.1 C of S/Cu_{1.8}Se electrodes. (e) Photograph of an electric fan with an "I LOVE YOU" pattern being charged by Li-S cells based on S/Cu_{1.8}Se electrodes. (f) Decay rate per cycle compared with other reported works.

Abstract Graphics

